A&A 467, 737–747 (2007)
DOI: 10.1051/0004-6361:20066626

Astronomy & Astrophysics

3.2 mm lightcurve observations of (4) Vesta and (9) Metis with the Australia Telescope Compact Array

T. G. Müller[1] and P. J. Barnes[2]

[1] Max-Planck-Institut für extraterrestrische Physik, Giessenbachstraße, 85748 Garching, Germany
e-mail: tmueller@mpe.mpg.de
[2] School of Physics A28, University of Sydney, Sydney NSW 2006, Australia
e-mail: peterb@physics.usyd.edu.au;

Received 24 October 2006 / Accepted 8 March 2007

ABSTRACT

Context. (4) Vesta and (9) Metis are large main-belt asteroids with high albedos. There are strong indications for heterogeneous surfaces for both targets from imaging techniques in the visible and near-IR range, very likely connected to impact structures. Despite that, the thermal spectral energy distributions from mid-IR to the mm-range have, until now, been consistent with a homogeneous regolith-covered surface and the thermal light-curves are dominated by the shape and spin vector properties.
Aims. With millimetre-observations at 93.0 and 95.5 GHz we tried to characterise the emission properties of the surface material. The coverage of the full rotation period allowed a detailed study of the heterogeneity of the surface.
Methods. We combined our carefully-calibrated mm-observations with sophisticated thermophysical modelling techniques. In this way it was possible to derive emissivity properties and to disentangle the effects caused by shape, albedo or various thermal properties.
Results. The rotationally averaged fluxes are explained very well by our thermophysical model techniques when using an emissivity in the mm-range of about 0.6 for (4) Vesta and about 0.7 for (9) Metis. The mm-lightcurves follow for a large fraction of the rotation period the shape-introduced variations. The rotational phases with clear deviations are connected to structures which are visible in the HST images of (4) Vesta and the Keck AO-images of (9) Metis. The observed lightcurve amplitudes are peak-to-peak ∼30% for (4) Vesta and ∼25% for (9) Metis, while the shape-related amplitudes are only 5 and 4%, respectively.
Conclusions. The emissivities at mm-wavelengths are lower than in the far-IR, confirming that particles with sizes of about 100 μm influence the mm-behaviour. Previously identified bright spots at visible/near-IR wavelength are connected to sharp emissivity drops. The dark Olbers region on (4) Vesta causes an excess in mm-emission on top of the shape introduced light-curve. The thermophysical model predictions match the overall flux levels very well, but cannot reproduce certain lightcurve features due to the lack of information on the grain size distribution. The 3-mm observations are very powerful for the study of surface heterogeneities.

Key words. minor planets, asteroids – radio continuum: solar system – infrared: solar system – techniques: photometric – radiation mechanisms: thermal

1. Introduction

(4) Vesta and (9) Metis are large main-belt asteroids with well-characterised shape, spin-vector, size and albedo properties (e.g., Thomas et al. 1997; Torppa et al. 2003; Storrs et al. 1999; Marchis et al. 2006). Both high-albedo targets also have indications of albedo variations on their surfaces (Binzel et al. 1997; Nakayama et al. 2000; Marchis et al. 2006).

(4) Vesta is a V-type asteroid and it is believed to be the parent body of the Vestoids (Binzel & Xu 1993). Radioisotope chronology from the howardite, eucrite, and diogenite (HED) meteorites is correlated with a (4) Vesta origin. Most importantly (4) Vesta has experienced significant excavating events, most notably indicated by the huge crater near its southern pole (Thomas et al. 1997). It is the first of the two asteroid targets to be visited by DAWN (http://dawn.jpl.nasa.gov/; Vernazza et al. 2005). (4) Vesta's visual lightcurve is dominated by the influence of the albedo variations and standard lightcurve inversion techniques failed to produce a reliable shape model (Kaasalainen, priv. comm.), but high resolution HST imaging allowed a solution for the shape and spin vector (Thomas et al. 1997).

(9) Metis is an S-type asteroid, which indicates a silicate and metal rich composition, mainly olivines, pyroxenes and metals in various percentages. Spectrophotometric similarity with (113) Amalthea revealed a probable compositional link between these two objects. A plausible common parent body was estimated to have been between approximately 300 and 600 km in diameter (Kelly & Gaffey 2000), but the search for nearby companions and family members was not successful (Storrs et al. 2005). Sophisticated lightcurve inversion techniques allowed a solution for a shape and spin vector which fits nicely the available visual lightcurves (Torppa et al. 2003). The shape and spin-vector solution is also in excellent agreement with adaptive optics images presented by Marchis et al. (2006). However, those authors noticed very strong intensity variations on the surface, but attributed them mainly to changing surface scattering properties.

Both targets were extensively observed at various wavelengths during the last decades. For (4) Vesta there are also a large number of thermal observations from IRAS (Tedesco et al. 2002a), ISO (Müller & Lagerros 1998, abbreviated as M&L 1998 in following) and also at sub-millimetre and millimetre wavelength (e.g., Redman et al. 1998), while for (9) Metis the infrared observations are limited to very few ISO (M&L 1998)

and MSX observations (Tedesco et al. 2002b). Due to their size and proximity both main-belt asteroids are bright at millimetre-wavelengths and easy to observe.

Our main objective was to obtain high-quality measurements of the 3 mm flux density of large main-belt asteroids over their full rotation period. Since the mm-lightcurves are not very much affected by albedo variations on the surface, we wanted to see and confirm if the shape model can explain possible brightness variations. As a second goal we were interested in the mm-emissivities of such bodies. Redman et al. (1992) reported a very low submm/mm-emissivity for (4) Vesta and interpreted their findings with the presence of a dusty, porous regolith. How does the emissivity compare at 3 mm? Furthermore, is the emissivity of (9) Metis, which has also a high albedo, comparable to that of (4) Vesta?

Johnston et al. (1989) performed microwave observations of (2) Pallas, (4) Vesta and (10) Hygiea. They concluded that the behaviour of these targets at cm-wavelengths is dominated by a layer of material with the physical properties of finely divided dust. They proposed to use mm-observations to identify those areas with different regolith properties, reflected in a rotational phase dependence of the brightness temperatures. We present now for the first time such rotationally resolved mm-observations. The data analysis and calibration are given in Sect. 2 and the observational results in Sect. 3. We applied a thermophysical model to our observations and derive the important thermophysical quantities. The methods used are described in Sect. 4. In Sect. 5 we combine the TPM predictions and the observations and discuss the possible implications.

2. Observation and calibration

Observations of (4) Vesta and (9) Metis were conducted at the Australia Telescope Compact Array (CA)[1] on 2004 October 13. The relevant observational details are summarised in Tables 1 and 2.

At the time of observation, five of the CA's six antennas had been equipped with receivers for the 3 mm band (the sixth antenna was not so equipped because of its fixed location at the 6 km station, too far to obtain correlated signals at 3 mm at this site). Because obtaining the most accurate flux densities was our primary goal, we paid very careful attention to all known calibration issues. We chose the maximum possible bandwidth available for each of two intermediate frequencies (IF) in the local oscillator (LO) chain; the receiver electronics allowed these two IFs to be up to 2.7 GHz apart, and so we chose to centre them at 93.0 and 95.5 GHz, with a view to possibly detecting an emissivity variation over this frequency range (see below). The frequencies in the mid-90s were chosen to maximise the overall sensitivity of the CA in this band. The pointing was checked approximately every hour, with corrections to each antenna's pointing table typically only a few arcseconds. For bandpass calibration we chose one of the brightest 3 mm point sources available in the southern sky (B1921-293, about 15Jy at this wavelength). We used Uranus as our absolute flux calibrator since its mm-wave emission appears to be well-matched by a simple uniform-disc model (Griffin & Orton 1993). This model gives 132.5 K for Uranus' brightness temperature at 94.25 GHz, which yields a zero-spacing flux density of 8.6 Jy at the epoch of observation. Thus, issues of pointing, bandpass calibration, or planet-based absolute flux scale calibration contributed negligibly to the overall error budget (see Table 3).

[1] The CA is a part of the Australia Telescope, which is funded by the Commonwealth of Australia for operation as a National Facility managed by CSIRO.

Table 1. Technical observing details.

Observatory	ATCA, Narrabri NSW
Longitude	149°32′56.327″ E
Latitude	30°18′52.048″ S
Altitude	209.3 m
Number/size of antennas	5 × 22 m
Antenna configuration	H214C
Physical baselines	10 (from 82 to 247 m)
UT date, time	2004 Oct. 13, 07:50–16:30
Precipitable water vapour	10–12 mm
Receivers	dual SIS
System temperatures	200–350 K
T_{sys} method	chopper wheel (Kutner & Ulich 1981)
Observing frequency (2 IFs)	93.0 and 95.5 GHz
Primary beam FWHM	35 arcsec
Pointing uncertainty	<5 arcsec
Total bandwidth	2 × 128 MHz
Channels per IF	32
Usable bandwidth	2× (29 ch) = 116 MHz
Polarisations	2 orthogonal, linear
Sample time	30 s
Bandpass calibrator	B1921-293, 10 min
Flux calibrator	Uranus, 10 min
Gain (amplitude & phase) cal.	B2345-167
Total integration time	(4) Vesta: 48 min (9) Metis: 291 min
Projected baselines	75 m to 245 m 22 to 75 kλ
Synthesised beam	∼3 arcsec
Observation cycle	i) point/T_{sys}: 2 min ii) phasecal B2345-167: 3 min iii) (4) Vesta: 3 min iv) (9) Metis: 19 min
Number/times of cycles	15× (29 min 30 s)

Table 2. Observation geometry at 2004-Oct-13 13:00 UT as seen from the CA site.

Asteroid	r [AU]	Δ [AU]	α [°]	$\lambda - \lambda_{sun}$ [°]
(4) Vesta	2.397416	1.525840	14.57	142.79
(9) Metis	2.276962	1.392145	14.86	144.16

The main calibration issues at mm wavelengths are the medium-term (∼hours) variability in the complex receiver gains, the atmospheric opacity, and the antennas' gain vs. elevation. Therefore periodic gain (amplitude and phase) calibration was performed using B2345-617, which was located 6.5° east of (4) Vesta at the time of observation. Since (9) Metis was itself only 2.5° north of (4) Vesta at this time, we were assured of obtaining an accurate *relative* calibration between the quasar and the two asteroids, even if the anennas' gain-elevation dependence (see below) was not well characterised.

From very simple model calculations, we anticipated (4) Vesta and (9) Metis would have 3.2 mm flux densities on this date of roughly 200 and 20 mJy, respectively. In this case we would have ideally achieved similar signal-to-noise measurements of their rotationally-averaged brightnesses by integrating on them in time in the inverse-square of this ratio, or ∼1:100. However, a more practical integration-time ratio turned out to be ∼1:6. The relative uncertainties of individual cycles are mostly statistical and we obtained roughly a S/N of 24 for Metis and 42

Table 3. Measured flux density RMS errors (per baseline unless otherwise noted).

RELATIVE UNCERTAINTIES:	
Thermal noise in asteroid signal (per cycle, both IFs and polarisations): V, M	10%, 15%
Loss due to pointing errors (3 arcsec)	0.3%
Bandpass calibration (B1921-293)	1%
Atmospheric opacity calibration	2%
Intercycle gain stability (after applying gaincal corrections),	2%
Intercycle phase stability (after applying gaincal corrections)	2° (typical) 10° (extreme)
Net relative uncertainty, per 30 min cycle, per baseline: V, M	10%, 15%
Net relative uncertainty per cycle, all baselines combined: V, M	3%, 5% (typical) 20% (extreme)
ABSOLUTE UNCERTAINTIES:	
T_{sys} temperature scale (chopper wheel vs. skydip methods), per antenna	5%
Gain elevation systematic errors	10%
Uranus model (132.5 K uniform disc)	2%
Total (absolute + relative) uncertainty, all times, all baselines combined	11%
per 30 min cycle	25% (extreme)

for Vesta per cycle. For the global average of the 15 cycles, the standard errors in the mean (SEM) do not average down by a factor of 4 because both lightcurves contain a number of points at large excursions from the mean, relative to the size of the error bars. Given the measured flux densities, uncertainties, lightcurve excursions, an so on, this time ratio serendipitously gave a relative $S/N \sim 35$ for both bodies.

To simultaneously obtain (a) the best calibration, (b) roughly equivalent *S/N* for both asteroids, and (c) time-resolved 3.2 mm lightcurves, we interleaved observations of our two asteroids in time. We set up our observe "cycle" as follows: (i) start with a pointing check and/or T_{sys} calibration, typically taking 2 min; (ii) observe the gain calibrator for 3 min; (iii) observe (4) Vesta for 3 min; and (iv) observe (9) Metis for 19 min. Each of these cycles thus took close to 30 min to execute, including time for telescope moves. After starting with the bandpass calibrator and Uranus, this observe cycle was executed 15 times over the 7.5 h span of the observations, finishing with an extra observation of the gain calibrator.

The post-observation calibration procedure followed standard CA practices, as implemented in the Miriad software package (Sault et al. 1995). The spectral bandpass in both the 93.0 and 95.5 GHz IFs was derived to high precision from the B1921-293 data. Variations in the receiver complex gains and atmospheric opacity and phase variations were simultaneously removed using B2345-167, a nearby 3 mm point source. This step puts B2345-167 and all the asteroid data on the same relative flux scale, and also removes any residual effects from inaccuracies in the gain-elevation correction for each antenna. If this has been done well, any remaining fluctuations or uncertainties should be dominated by thermal noise from the atmosphere + antenna + receiver system, and this indeed seems to be the case for most of our data (see Table 3, "relative uncertainties").

However, for a couple of the cycles, the system phase stability was much more erratic than normal (labelled "extreme" in Table 3). In the case of the last cycle (16:00 < UT < 16:30), this was likely due to the low elevation of our sources (~30°), and consequent variability in atmospheric opacity. For the second cycle (9:45 < UT < 10:15), its cause was less obvious (being at elevation ~50°), but may have been similarly due to short-term atmospheric changes. Such phase fluctuations have the effect of decorrelating the visibilities from the source, and reducing their observed amplitudes. However, the gain calibration seemed to compensate adequately for this, by boosting the scalar amplitudes of the visibilities an appropriate amount. The result is that the vector-averaged visibilities during such episodes are brought into line with those from more stable cycles. However, we return to this issue when discussing the asteroids' light curves below.

For absolute calibration, this is first done approximately by converting the data to the T_{sys} temperature scale. Note that the data are split up into 4 independent parts, namely the *XX* and *YY* correlations for both the 93.0 and 95.5 GHz IFs. These are independent of each other since each antenna has two receivers sensitive to orthogonal linear polarisations from the sources, and the frontends (which are broadband devices) have their upper and lower IF signals split in the LO chain and admitted to separate halves of the correlator. Thus there are four independent T_{sys} measurements made at the start of each observe cycle. These temperature scale measurements are thought to be reliable to ~5%, based on comparisons between the chopper-wheel method of Kutner & Ulich (1981), which is the standard method used at the CA, and skydip measurements also performed at the CA by R. Sault (private communication).

While the *XX* and *YY* data for each frequency should be giving us the same result for an unpolarised source, and this appears to be the case here, the two IFs may give different amplitudes. This can be due not only to the receivers' broadband sensitivity as a function of frequency, but also to the intrinsic spectral index of the source. Thus any differences between the two IFs are not significant until we have bootstrapped the data to an absolute flux scale. To disentangle these two effects, at 3 mm we observe a source with a known flux density at the frequencies of interest, such as a planet. Normally, the average of the corrections from the gain calibrator are applied to the planet data, which are then compared to a planet model, and a simple, single scaling factor derived to correct from the relative to the absolute scale. The correction factor is then applied to the gain calibrator and source data.

However, since the CA's new 3 mm system had only recently been commissioned at the time of observation, the correction for each antenna's gain as a function of elevation above the horizon had not yet been well-characterised. This is significant since a poor gain-elevation correction can masquerade as a variation in the antenna-based receiver gain correction. By itself, this will be removed by using the gain calibrator to nevertheless give a good relative flux scale. But, if the flux calibrator is not observed *at the same time and elevation* as the gain calibrator, it will not be

possible to differentiate between a poor gain-elevation correction and a genuine reciver-gain drift. This can potentially result in large errors in determining the absolute flux scale, of up to 50% (Klamer, private communication), even while the relative flux scale is quite accurate.

This problem is worst when the flux calibrator is observed at an elevation which doesn't correspond to any programme source elevations. In such cases the absolute flux scale essentially has to be guessed. Fortunately in our case, Uranus was observed at around 57° elevation, close to the mean elevation of our sources (between 27° and 75°, see also Table 4), which means correcting for this effect is at least possible, and moreover should constitute a small effect. Nevertheless, instead of using the time-averaged gains from our gain calibrator (i.e. data from all elevations) to apply to Uranus, we used only the corrections from when B2345-167 was very close to the elevation (57°) at which we observed Uranus. This means that whatever the gain-elevation correction *should* have been for our data, any erroneous effect on our absolute flux scale was completely removed from the data. The only remaining calibration issue was a roughly 2-h gap between the Uranus observations and the commensurate B2345-167 observations (made before transit), during which time the receiver gains would have slowly drifted by an unknown amount. However we also observed B2345-167 about four hours later (after transit) at the same elevation, where we could see that the gain corrections had not significantly changed from the before-transit numbers, to within a ∼10% level. Based on this, we put the overall gain uncertainty due to this effect at 10%, although it may be significantly less than this.

This uncertainty by far dominates our error budget for the absolute flux densities (Table 3). However, now knowing the nature of the effect, it should be possible in future projects at the CA to reduce this uncertainty to perhaps 5% or less, by a more timely planet observation, or by several observations spread over a range of elevations. Despite all this, we emphasise that our relative flux scale (i.e., between the gain calibrator and the asteroids, between the two asteroids, or within a single asteroid's data) is good to ∼4% per cycle (all baselines combined), or ∼1% overall.

3. Observational results

We present our flux density measurements as a function of UT for (4) Vesta and (9) Metis in Figs. 1 and 2 and Table 4.

For large main-belt asteroids the Standard Thermal Model (STM, Lebofsky et al. 1986) is generally used to estimate flux densities. Applying the STM with the default parameters for beaming, emissivity and phase angle corrections resulted in a flux of 212 mJy for (4) Vesta and 22.6 mJy for (9) Metis using the best published size and albedo values (see Sect. 4 for the detailed values and the references). The first remarkable result of our data is that the 3.2 mm flux density of (4) Vesta is about 30% less, and of (9) Metis roughly 50% higher, than that expected from the simple STM predictions. Given the discussion above about relative and absolute flux calibration, we regard these results as fairly robust. For example, if the absolute flux scale is systematically wrong (due, e.g., to a gain drift between the Uranus and B2345-167 observations which was larger than the 10% assumed), it is conceivable that one or other of the asteroids' flux densities could be brought into line with the prediction from the STM, but not both at once. Thus the mean ±SEM (standard errors in the mean) 3.2 mm flux ratio (9) Metis/(4) Vesta is more than double the prediction of the STM of a ratio ∼0.1 (see Table 5).

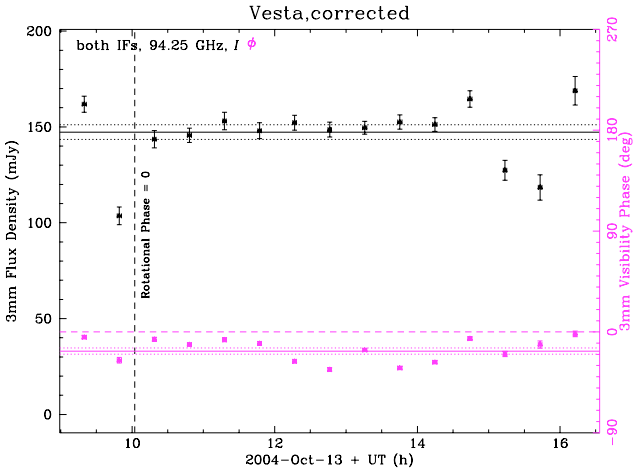

Fig. 1. (4) Vesta 3.2 mm flux density S_I of total intensity (visibility amplitudes in black, visibility phases in magenta) vs. UT. Each data point represents a vector average of several 30-second samples covering an observing cycle, each sample being itself a vector average over (i) 29 × 4 MHz channels in the correlator, (ii) 2 linear polarisations (designated *XX* and *YY*), (iii) 2 IFs (93.0 and 95.5 GHz), and (iv) 10 baselines, or 1160 correlations per sample. The error bars in time simply bracket the range of UT over which the samples were taken (5 or 6 samples per cycle in the case of (4) Vesta). The flux error bars are the standard errors in the mean (SEMs) from the vector average of the samples, i.e., the rms. of the vector average, divided by the square root of the number of correlations that went into the average: the larger the errorbars of a plotted point, the more unstable were the data that went into that average. The horizontal solid and dotted lines represent the mean ±SEM (respectively) of all data.

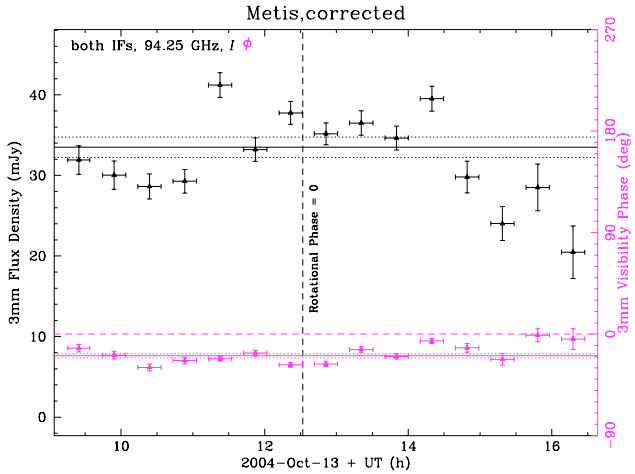

Fig. 2. (9) Metis 3.2 mm S_I vs. UT, otherwise the same as Fig. 1. The (9) Metis data have about 38 samples per cycle, hence the larger time error bars than in Fig. 1.

Upon further inspection, there is a suggestion in the data of significant 3.2 mm lightcurves for both asteroids. In (9) Metis' case, the variation over the asteroid's sidereal period of 5.079 h appears to be large (±12% around the mean) and sinusoidal (see Fig. 3). This suggests a significant hemispherical difference in the 3.2 mm emissivity of this body. The sinusoid seems to persist in whatever division of the data we plot: total intensity (Fig. 3), or split by polarisation, frequency, or both (Fig. 4a–c). The sinusoid also seems to be reproduced by data taken at different UT but the same rotational phase. In light of the small relative and absolute uncertainties in the flux density scale, all these

Table 4. ATCA calibrated flux densities for an average frequency of 94.25 GHz (3.18 mm) as a function of time. The corresponding rotational phases are also given (based on rotation periods of 5.34 h for (4) Vesta and 5.08 h for (9) Metis together with specific zero points, see Sect. 4). Note, that the errors given are the relative uncertainties which are dominated by the thermal noise. For a better judgement of the errorbars, the observed elevations are also given.

Julian Date	FD [mJy]	Error [mJy]	Rotational phase [°]	Obs. elev. [°]
(4) Vesta				
2 453 291.88872	161.8	4.2	312.38	51.4
2 453 291.90920	103.6	4.6	345.51	57.4
2 453 291.92969	143.6	4.5	18.64	63.4
2 453 291.95017	145.6	3.8	51.77	68.4
2 453 291.97066	153.1	4.6	84.91	72.5
2 453 291.99115	148.0	4.2	118.05	74.6
2 453 292.01163	152.2	3.9	151.17	74.0
2 453 292.03212	148.6	3.9	184.31	70.8
2 453 292.05260	149.6	3.4	217.43	66.1
2 453 292.07309	152.6	3.8	250.57	60.6
2 453 292.09358	151.3	3.6	283.71	54.7
2 453 292.11406	164.6	4.3	316.83	48.6
2 453 292.13455	127.4	5.2	349.97	42.4
2 453 292.15503	118.4	6.6	23.09	36.1
2 453 292.17552	168.9	7.5	56.23	29.7
(9) Metis				
2 453 291.89219	31.9	1.8	138.99	51.2
2 453 291.91267	30.0	1.8	173.82	57.1
2 453 291.93316	28.6	1.5	208.68	62.6
2 453 291.95365	29.3	1.5	243.53	67.3
2 453 291.97413	41.2	1.5	278.37	70.8
2 453 291.99462	33.2	1.5	313.23	72.3
2 453 292.01510	37.8	1.4	348.06	71.2
2 453 292.03559	35.2	1.4	22.92	68.0
2 453 292.05608	36.5	1.5	57.77	63.4
2 453 292.07656	34.6	1.5	92.61	58.0
2 453 292.09705	39.5	1.6	127.47	52.2
2 453 292.11753	29.8	2.0	162.30	46.2
2 453 292.13802	24.0	2.1	197.16	40.0
2 453 292.15851	28.5	2.9	232.01	33.7
2 453 292.17899	20.5	3.3	266.85	27.4

features strongly suggest that the effect is real. The parameters of the sinusoidal fit, of the form

$$S(\phi) = S_0[1 + A \sin 2\pi(\phi - \phi_0)] \quad (1)$$

(where S is the flux density at rotational phase ϕ [measured in units of the rotational period P], S_0 is the rotationally-averaged mean flux density, A is the amplitude of the sinusoid, and ϕ_0 is the phase offset [also measured in units of P]), are given in Table 5. All results quoted in Table 5 are from weighted least-squares fits to the individual cycle data points, and where the weight for each point was taken as its $(\mathrm{rms})^{-2}$.

For (4) Vesta, we also see lightcurve variations over this body's 5.342 h sidereal period. A strong dip ~25% below the mean flux density (near $\phi \sim 0.95$) appears in total intensity (Fig. 5). The dip becomes somewhat less convincing in the frequency- or polarisation-split data (Fig. 6a–c), but is still present. Bright spikes in (4) Vesta's lightcurve to either side of the dip (near $\phi \sim 0.87$ and 1.15) can also be seen. These features do seem to repeat from one rotation to the next, and are not confined to only those cycles which experienced extreme phase instability[2] (see Sect. 2). This suggests the dip and spikes may not simply be artefacts of anomalous phase errors in some of the data. But since their existence is not easy to explain, their reality should be confirmed by future experiments. Parenthetically, it is worth noting that for the flat part of (4) Vesta's lightcurve (10:15 < UT < 14:15, Fig. 1; or $0.2 < \phi < 0.8$, Fig. 5), the fluctuations are entirely consistent with thermal noise.

[2] The larger the errorbars of a plotted point, the more unstable were the data that went into that average.

Table 5. ATCA calibrated flux densities, spectral index, colour (rotationally averaged). The errors given correspond the statistical uncertainties. As specified in Table 3, the total absolute flux error is around 11%. The coefficients are specified for the sinusoidal fit $S(\phi) = S_0[1 + A \sin 2\pi(\phi - \phi_0)]$.

		(4) Vesta	(9) Metis
$S_0 \pm SEM$	all data	147.3 ± 3.8 mJy	33.5 ± 1.0 mJy
	93.0 GHz	147.3 ± 3.8 mJy	32.4 ± 1.1 mJy
	95.5 GHz	147.5 ± 4.8 mJy	34.6 ± 1.2 mJy
Sinusoidal fit: $A \pm SEM$		<±5%	12% ± 3%
$\phi_0 \pm SEM$		–	–0.175 ± 0.05
Spectral index $\alpha \pm SEM$		0.1 ± 1.6	2.5 ± 1.8
3.2 mm "colour" ± *SEM*		–1.9 ± 1.6	+0.5 ± 1.8
M:V flux ratio ± *SEM*		0.224 ± 0.009	

Returning to (9) Metis, we see some similarly interesting deviations from the fit sine curve. Most notably, at $\phi \sim 0.75$ data from two different rotations appear completely inconsistent. The lower point at ~20 mJy might be easily explained away as an artefact of the extreme phase variations during the last cycle (UT ~16:20), insufficiently calibrated. However the upper point at ~41 mJy (UT ~ 11:20, cycle 5) is not so easily dismissed. The separate data for this point in Fig. 6c are very tightly grouped, giving a point in total intensity (Fig. 5) standing ~5σ above the fitted sine curve. So while this makes the spike appear real, it is hard to imagine a surface feature that could give rise to it. Perhaps more likely is a ~10 min long atmospheric phase decorrelation episode during the gaincal measurement before cycle 5, and during the cycle-5 measurement for (4) Vesta, which then ended for the cycle-5 measurement of (9) Metis. This would result in a correctly-compensated cycle-5 value for (4) Vesta, but an over-corrected cycle-5 value for (9) Metis. Whether or not this explanation is correct, averaging in the low cycle-15 point to the high cycle-5 point for (9) Metis would bring the mean of the two points at $\phi \sim 0.75$ very close to the fitted sine. Either way, without these two cycles, the rest of the (9) Metis data are again consistent with thermal noise around the sine curve.

A third interesting result for these bodies is the evidence in the data for different spectral indices at 3.2 mm (or equivalently, emissivity variations, or "3.2 mm-colours"). Despite the issues with the absolute flux scale discussed above, the relative calibration between the two IFs at 93.0 and 95.5 GHz should be good to the level in Table 3 quoted for the relative flux scale, since whatever effect receiver-gain drifts and the gain-elevation correction have on our data, they are likely to be very similar for the two IFs. We define the spectral index α between two frequencies by $S(\nu) \sim \nu^{\alpha}$; then a roughly 200 K blackbody (or grey-body) should have $\alpha = 2.0$ at these frequencies, being in the Rayleigh-Jeans tail of the Planck function. This allows us to also define the "3.2 mm colour" as $\alpha - 2$. From Figs. 4a and 6a we obtain the values for α and the 3.2 mm colour in Table 5. Put another way, (9) Metis' 3.2 mm colour is consistent with a grey body, while (4) Vesta's 3.2 mm colour is much "redder" than a grey body. The uncertainties are fairly large, however, due to the small frequency range (3%), so these results must be treated as fairly tentative, although the appearance of different colours for the two asteroids is unlikely to be due to a *systematic*

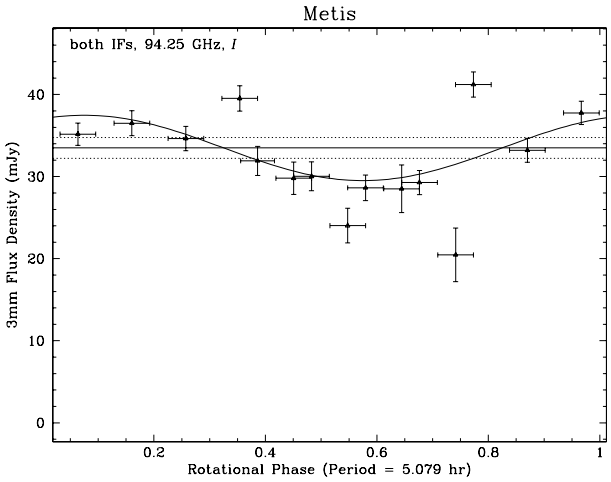

Fig. 3. (9) Metis total intensity I vs. rotational phase ϕ. The curve is for the best fit sinusoid described in the text. In Figs. 3 and 4, the zero of ϕ is taken at 2004-Oct-13 12:31:51 UT. The other features are the same as in Fig. 1.

instrumental effect. Moreover, the errors for the spectral index quoted in Table 5 overstate the uncertainty. Omitting the Olbers-related data points (see below) from Vesta's lightcurve, these SEMs are reduced by a factor ∼3. If confirmed, these 3.2 mm colours suggest that while (9) Metis' emissivity is roughly constant around 3 mm, (4) Vesta's emissivity might actually be rising towards longer wavelengths. We return to this issue in Sect. 5.

In contrast, we note there *is* a residual instrumental effect visible in the polarisation split data (Figs. 4b, 6b). For both (4) Vesta and (9) Metis at both frequencies, the *XX* data appear to be systematically brighter than the *YY* data before transit, and systematically fainter after transit. The difference in all cases is at a level of ±5%, and seems to be related to a similar effect appearing also in the gain calibrator data. For B2345-167, the *XX*-*YY* difference before and after transit was around ±15%, although this was calibrated out as part of the normal data reduction. This similarity might be explained, for example, if there was a real difference in the gain-elevation correction for the two polarisations, perhaps as a result of some differential flexure in the optical path for the two receivers as the antennas tracked the calibrator and sources at slightly different elevations. This is a fairly unlikely explanation, however, and is more likely just due to the fact that the instrumental polarisation at 3 mm had not yet been determined at the time of our observations. With proper polarisation calibration, future experiments at the CA may well enable all the Stokes parameters I, Q, U, and V to be measured at 3 mm.

Finally, we point out that the asteroid phases (Figs. 1 and 2) centre around –17° and –20° respectively for (4) Vesta and (9) Metis. It is most probable that these non-zero phases indicate a shift in each asteroid's position from the ephemeris-determined phase-pointing centre. With synthesised beams around 3″, the positional shifts corresponding to these phases would be around a tenth of this figure, or 0.3″. This angle also roughly corresponds to each asteroid's subtended diameter as viewed from Earth at the time of observation (0.238″ for (4) Vesta, 0.170″ for (9) Metis). Ephemeris uncertainties are even smaller, about a tenth of the diameters.

In the absence of more reasonable explanations, these non-zero visibility phases are possibly due to a combination of two effects: a hint of a 24-h variation about the zero visibility phase

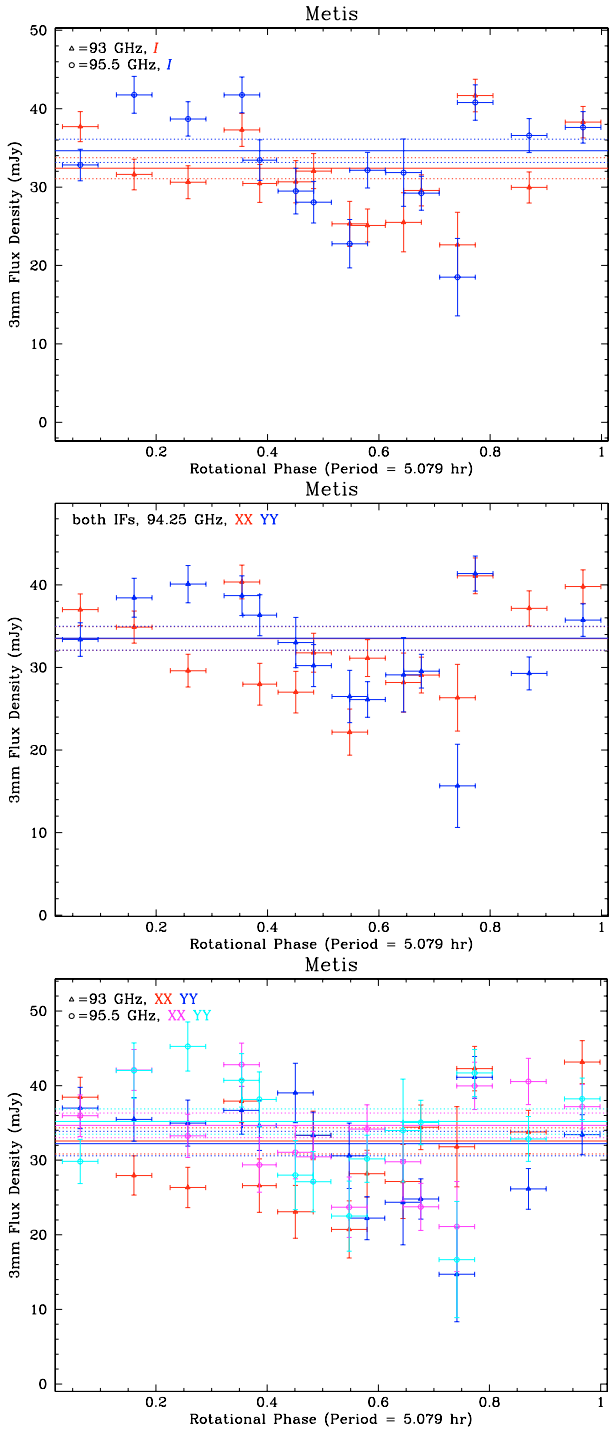

Fig. 4. Subsets of the data from Fig. 3. **a)** (9) Metis I-93 and I-95.5 GHz vs ϕ; each frequency is averaged over both polarisations. **b)** (9) Metis *XX* and *YY* vs. ϕ; each polarisation is averaged over both frequencies. **c)** (9) Metis data vs ϕ; each frequency-polarisation subset is split out separately.

due to a slight error in the baseline solution, and in Vesta's case at least, a 5-h variation about the mean visibility phase. This number, if real, seems inescapably connected to the body itself. It is as if bright or dark features are rotating into and out of view about the centre of the body, giving an apparent shift in the mean position of (4) Vesta, lending further credence to the interpretation of the lightcurve variations as being due to surface emissivity features (see Sect. 5). If improvements to the CA's

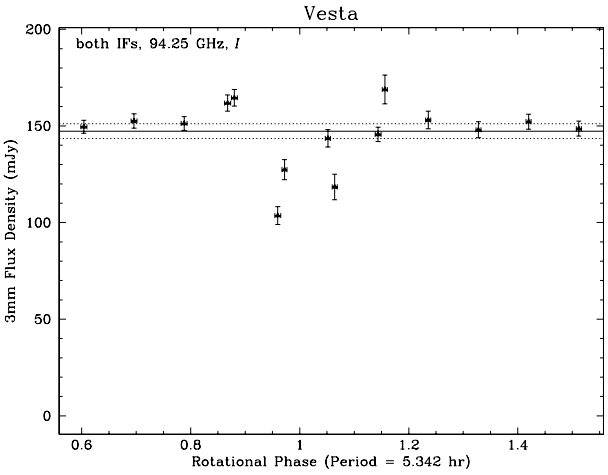

Fig. 5. (4) Vesta I vs. ϕ, otherwise the same as for Fig. 3. For (4) Vesta the zero of ϕ is taken at 2004-Oct.-13 10:02:10 UT (here and also in Fig. 6).

performance at 3mm, such as implementing some kind of phase-tracking scheme, can be made in the future, the possibility exists of directly imaging at 3 mm some of the larger asteroids at an apparition's perigee using baselines ~3 km. For asteroids such as Ceres or Pallas, this would allow spatially resolved modelling of the regolith properties over their surfaces.

4. Thermophysical modelling

A recent thermophysical model (TPM) describes the thermal emission of asteroids, including size, shape, albedo, rotational, surface regolith and thermal behaviour aspects (Lagerros 1996, 1997, 1998). We used this TPM together with the best available shape models and spin vector solutions (see Tables 6 and 7). The values of the thermal properties are taken from M&L 1998, 2002, with a wavelength-dependent emissivity model, a thermal inertia of 15 J m^{-2} s$^{-0.5}$ K^{-1} and a "default beaming model" with $\rho = 0.7$ (the rms of the surface slopes) and $f = 0.6$ (the fraction of the surface covered by craters). The TPM beaming model accounts for the non-isotropic heat radiation, noticeable at phase angles close to opposition. The most critical parameters for absolute flux predictions at thermal wavelengths are the effective diameter and the albedo values of an asteroid and its emissivity (e.g., Müller 2002). They are discussed in more details in the subsequent sections.

4.1. Asteroid (4) Vesta

Thomas et al. (1997) derived the size of (4) Vesta from a series of HST images. The best fit was obtained by a triaxial ellipsoid of radii 289, 280 and 229 km (all ±5 km), specified in "note added in proof". This corresponds to an effective diameter of 529.2 km. Our best thermophysical model solution, based on more than 200 independent thermal observations in the mid-IR to mm-range, resulted in a slightly larger value of 541.0 km. The standard deviation of the radiometric solution is 28.8 km which brings both size values into agreement. Tedesco (1989) derived an average geometric albedo of 0.38 at 0.55 μm. From the most recent albedo value ($p_H = 0.370$) by Shevchenko & Tedesco (2006), we calculated a radiometric value of $p_V = 0.33 \pm 0.04$, again in agreement within the errorbars. Binzel et al. (1997) reported a low albedo feature on the surface (which they proposed

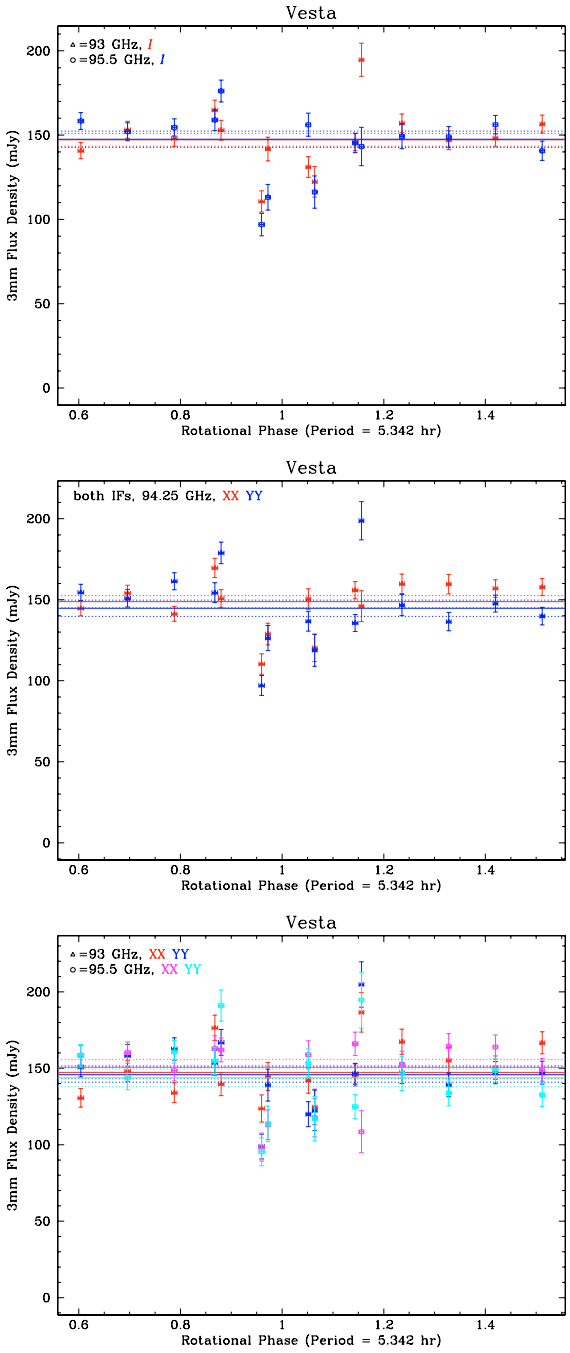

Fig. 6. Subsets of the (4) Vesta data from Fig. 5 vs. ϕ, otherwise the same as for Fig. 4.

to name "Olbers") with an estimated value of 0.3 at 0.439 μm, about 10–20% lower than the average at this wavelength.

We take the above full range of diameter/albedo values into consideration for the further analysis. We applied a (4) Vesta-specific wavelength-dependent emissivity as determined by M&L (1998) and in agreement with Redman et al. (1992). This emissivity model has values of around 0.6 in the submm-range and slightly larger values of around 0.7 at millimetre-range (see also Webster & Johnston 1989 for the slightly higher values at cm-wavelength). The translation into a temperature picture is shown in Fig. 7 for the specific observing and illumination geometry during the CA observations.

Table 6. Thermophysical model input parameter and resulting flux densities.

(4) Vesta	
H, G	3.20 mag, 0.34 (M&L 1998, refs. therein)
shape	Thomas et al. 1997 (HST observations)
SV and zeropoints	Thomas et al. 1997 (note added in proof)
Rot. period	0.2225887 days (Drummond et al. 1988)
ϵ-model:	$\epsilon = f(\lambda)$ (M&L 1998)
thermal inertia Γ	15 J m^{-2} s$^{-0.5}$ K^{-1} (Müller et al. 1999)
beaming parameter	$f = 0.6$, $\rho = 0.7$ (M&L 2002)
TPM predictions	
FD at 3180 μm	170 ± 8 mJy ($\epsilon(\lambda)$, M&L 1998)
at observation epoch	146 ± 8 mJy ($\epsilon(\lambda)$, but with
(rotation averaged)	$\epsilon \sim 0.6$ at submm/mm)
mm-lc amplitude	±4 mJy (=±2–3%)
TPM prediction	(shape-dominated)

Note: The implementation of the Thomas et al. (1997) shape model produces a zero rotational phase at 2004-Oct.-13 10:02:10 UT for the given spin vector (SV) and rotation period.

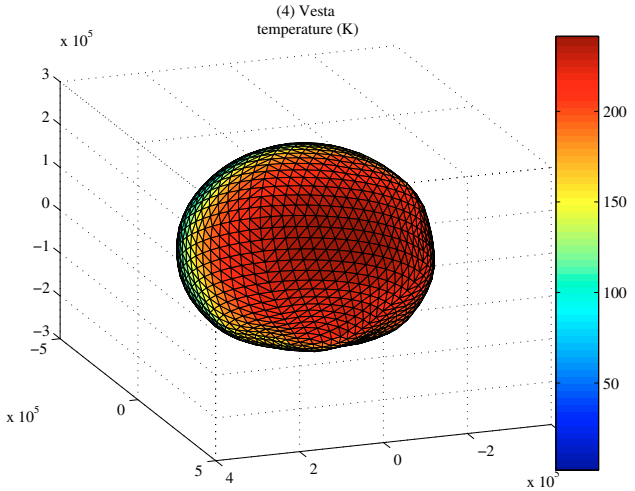

Fig. 7. Temperature distribution on the surface of (4) Vesta, based on the HST-shape model in combination with the thermophysical parameters and calculated for 2004-Oct.-13 09:00:00 UT.

Table 7. Thermophysical model input parameter and resulting flux densities.

(9) Metis	
H, G	6.28 mag, 0.17 (Lagerkvist et al. 2001)
shape	2040 trishape surface elements
	and 1022 vertices (Torppa et al. 2003)
Spin vector	β_P, λ_P, $P_{\rm sid}$ (hrs):
(Marchis et al. 2006)	21.17, 180.48, 5.07917628
Zeropoints	T_0, ϕ_0
(MK, priv. comm.)	2433222.66230, 270.0
ϵ-model:	$\epsilon = f(\lambda)$ (M&L 1998)
thermal inertia Γ	15 J m^{-2} s$^{-0.5}$ K^{-1} (Müller et al. 1999)
beaming parameter	$f = 0.6$, $\rho = 0.7$ (M&L 2002)
TPM predictions	
FD at 3180 μm	40 ± 4 mJy ($\epsilon(\lambda)$, M&L 1998)
at observation epoch	35 ± 3 mJy ($\epsilon(\lambda)$, but with
(rotation averaged)	$\epsilon \sim 0.7$ at submm/mm)
mm-lc amplitude	±1 mJy (=±2%)
TPM prediction	(shape-dominated)

Note: Our implementation of the Kaasalainen (priv. comm.) shape model produces a zero rotational phase at 2004-Oct.-13 12:31:51 UT.

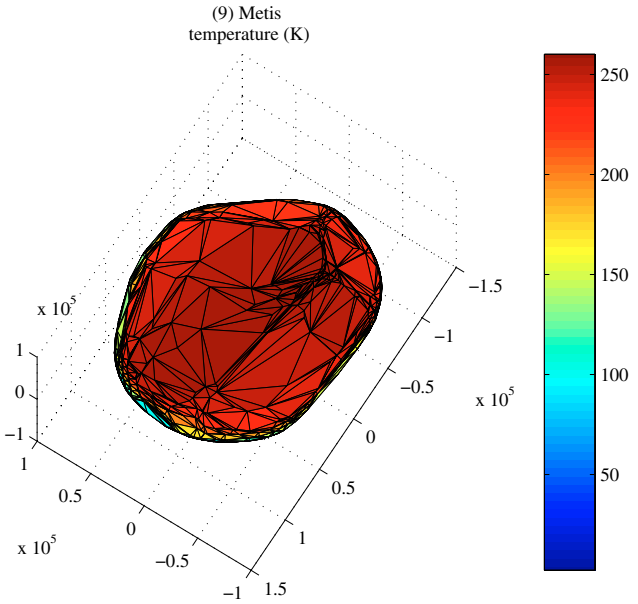

Fig. 8. Temperature distribution on the surface of (9) Metis, based on the shape model (derived from lightcurve inversion techniques) in combination with the thermophysical parameters and calculated for 2004-Oct.-13 09:00:00 UT.

4.2. Asteroid (9) Metis

Storrs et al. (2005) derived from WF/PC HST images a size of $222 \times 182 \pm 12$ km and an albedo of $p_{\rm V} = 0.108 \pm 0.006$. Tedesco et al. (2002b) calculated, via a simple radiometric method and from a one-epoch MSX measurement in 4 bands between 4.2 and 26 μm, an effective diameter of $D_{\rm eff} = 153.62 \pm 4.14$ km and an albedo of $p_{\rm H} = 0.2307 \pm 0.0123$. But both results, the HST and the MSX, are only related to an instantaneous cross section rather than a reliable effective size. Mitchell et al. (1995) combined radiometric, lightcurve and occulation data, resulting in a model ellipsoid of $215 \times 170 \times 135$ km (±15%). The corresponding effective diameter is $D_{\rm eff} = 2(abc)^{1/3} = 170.2$ km. We re-determined the diameter and albedo values using the Torppa et al. (2003) shape and spin vector in the TPM code together with the colour-corrected and calibrated MSX flux densities (Tedesco et al. 2002b), the ISO data point (Lagerros et al. 1999) and ground-based N-band ($\lambda = 7.5{-}14\,\mu$m) and Q-band ($\lambda = 16{-}28\,\mu$m) observations by Hansen (1976). The weighted mean values from our radiometric analysis are $D_{\rm eff} = 171.9 \pm 13.0$ km and $p_{\rm V} = 0.19 \pm 0.03$. The corresponding largest dimensions of the shape model are $218 \times 180 \times 129$ km, in excellent agreement with the numbers by Mitchell et al. (1995).

An independent confirmation of the albedo was published by Nakayama et al. (2000) based on photo-polarimetric observations over many phase angles. They derived an albedo of 0.15. Adaptive optic images of (9) Metis at 2 different epochs (Marchis et al. 2006) prove the good quality of the shape model. The AO average size of 181 km is also in agreement with our effective diameter value. Nevertheless, the irregular shape and the surface variegations are sources of uncertainties for the size as well as for the albedo values resulting from different techniques.

For our subsequent calculations we used an effective diameter of 176 ± 8 km and an albedo of 0.18 ± 0.04. We applied

the wavelength-dependent emissivity model for large regolith-covered asteroids as determined by M&L (1998). This emissivity model has values of 0.9 at mid-/far-IR wavelengths and 0.8 in the submm-/mm-range. Figure 8 shows the temperature distribution picture on top of the shape model for the epoch of the CA observations.

5. Discussion

5.1. Asteroid (4) Vesta

Based on the input parameters in Table 6 we obtained a 3180 μm flux density of 165...175 mJy, depending on the above albedo/diameter combinations. Lowering the mm-emissivity also to a value of 0.6 would give flux densities of 140–150 mJy (averaged over one rotation period). The albedo uncertainty does not affect the flux prediction very much (10% uncertainty produces a 1 mJy flux change). The diameter is more relevant: 2.5% uncertainty would bring both diameter solutions into agreement, but cause flux differences of roughly 5%, i.e., about 8 mJy (see Table 6).

The measured values favor therefore the solution with the lower emissivity at mm-wavelength, i.e., a constant low emissivity of around 0.6 at wavelengths between the submm-range and a few mm. In addition to our favoured solution (solid line in Fig. 9) we also show the best emissivity model for (9) Metis as a dashed line.

The TPM lightcurve amplitude calculation is shown in Fig. 9 together with the observed data points. This model lightcurve (solid line) is only reflecting the flux variation due to the change in cross-section during the rotation of (4) Vesta. There might be an additional component due to albedo variations, but even very strong variations could only produce very weak lightcurve features. A simulated dramatic albedo drop on one hemisphere from 0.35 to 0.20 would cause a flux change of about 3 mJy, still within the shape-introduced effects.

A lack of insulating dust regolith on some parts of the surface would have much more dramatic effects on the lightcurve: Under the given observing and illumination geometry the change from a thick dust layer with low thermal inertia to a rocky surface with high thermal inertia could lower the flux by up to 20 mJy. Such an effect might explain the reproducible flux drop in Fig. 9 (bottom). On the other hand, the thermal lightcurve at far-IR wavelength does not show any deviation from the shape-introduced lightcurve of that kind (B. Schulz, priv. comm.). Redman et al. (1992) found that the 1 mm light-curve is apparently dominated by the triaxial shape, without any significant contributions from the optical albedo spots. This excludes the theory of a pronounced change in the surface texture. But the solution could be in a change of the grain size distribution. Redman et al. (1992) showed that scattering by gains within the regolith can reduce the emissivity in a wavelength dependent fashion. This mechanism has also been proposed to explain the low apparent emissivity of the Moon (Simpson et al. 1981). The scattering becomes effective at wavelength shorter than $2\pi a$, with a being the grain size. Redman et al. (1992) speculated therefore that within (4) Vesta's regolith there must be a large population of particles around 100 μm in size. We would follow their interpretation except for the region on the surface which is responsible for the sudden flux drop in the mm-light-curve. At that position there must be a grain population with a predominantly larger particle size. Particles with sizes of several 100 μm would absorb more at mm-wavelengths without affecting very much the emissivity in the far-IR or submm-range. We believe that the larger particles might be related to a younger surface, possibly due to a recent impact. These particles are not yet processed by space weathering and impacts of micro-meteorites.

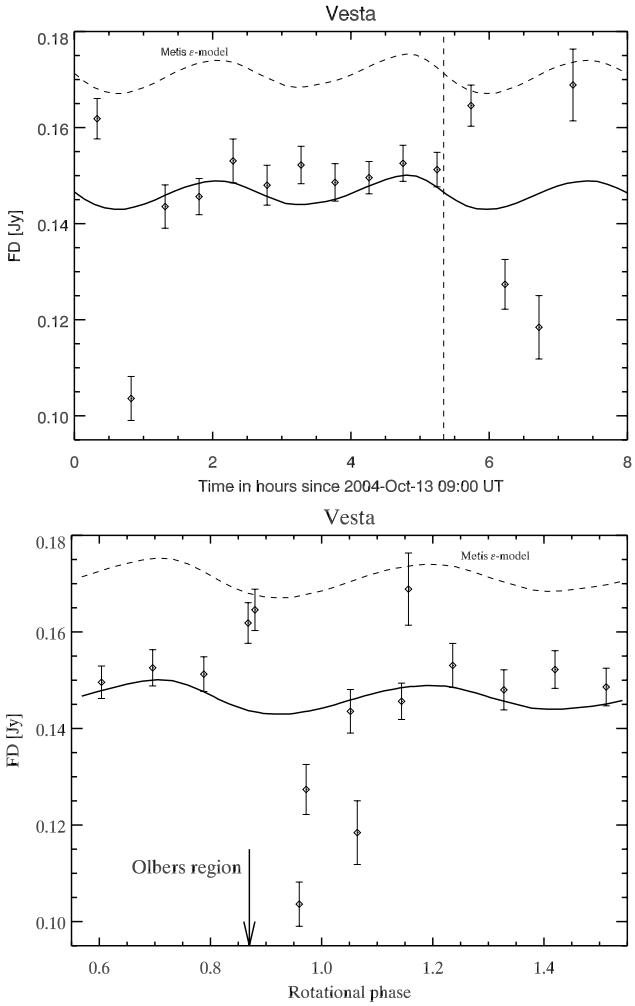

Fig. 9. *Top*: absolute flux prediction over time (solid line) together with the measurements (see Table 4). We used the lower emissivity of 0.6 at mm-wavelength together with a size of 535 km and an albedo of 0.35. The vertical dashed line indicates one rotational period. *Bottom*: the same as in the top, but now plotted against the rotational phase. For clarity reasons we show the data at rotational phases between 0.55 and 1.55, instead of [0,1]. The zero point in rotational phase is connected to the definition in Table 6. For the dashed lines we used the emissivity model for (9) Metis. The arrow refers to the rotational phase when the Olbers feature crosses the sub-Earth meridian.

Barrera-Pineda et al. (2002) also indicated that they saw at 870 μm a lightcurve with a 20% amplitude and which varied inversely to the visible lightcurves. Unfortunately, these observations are not publicly available for independent investigations and to separate shape and emissivity influences. From a comparision with the HST images of (4) Vesta by Thomas et al. (1997) they concluded that high temperatures are observed in regions of low albedo and low temperatures in regions of high albedo. Furthermore, they saw a marked difference in the thermal emission between the two "hemispheres" as outlined in the geologic maps of Binzel et al. (1997). These considerations make the hint of a rising emissivity for (4) Vesta (Sect. 3) all the more intriguing.

(4) Vesta's measured fluxes at 93.0 and 95.5 Ghz are the same (see Table 5), and so somewhat at odds with the notion of a grey body with a $S_I \propto \nu^2$ dependence as predicted by the TPM.

The TPM in fact predicts a roughly 8 mJy drop in (4) Vesta's flux from 95.5 to 93.0 Ghz. The red "colour" for (4) Vesta in Table 5 effectively means that (4) Vesta's low mm-emissivity might be rising again at longer wavelengths. In contrast, the frequency data for (9) Metis are entirely consistent with a grey body (constant emissivity) prediction from the TPM. If these 3 mm colours can be confirmed, it would mean that we could establish an upper limit for the particle size in the scattering regolith. What would be even more interesting is if we could see how the amplitude of (4) Vesta's lightcurve variations might change with wavelength, allowing us to conduct this analysis over different features of (4) Vesta's surface. However we emphasise that the detection of a rising emissivity for (4) Vesta towards longer wavelengths is marginal (a 1.2-σ result, or 3-σ away from Olbers), and needs to be confirmed.

Zellner et al. (1997) and Binzel et al. (1997) reported on basis of HST images of (4) Vesta a surface feature with lower albedo. They called it "Olbers" and they speculated that this might be related to (4) Vesta's ancient basaltic crust. The exact same rotational phase during our observations corresponds to the two fluxes well above the predicted lightcurve (at around rotatational phase 0.87 in Fig. 9 bottom). The low albedo, probably in combination with slightly different surface material properties, could explain the higher mm-fluxes. The strong flux drop in the lightcurve in Fig. 9 (bottom) occurs when the Olbers region has moved to the side by about 40° in rotational phase, i.e., at 1.0 in Fig. 9 (bottom). It might well be connected to the Olbers structure, e.g., ejecta material from an impact which is deposited only on one side of a crater. We cannot confirm a pronounced hemispherical difference as it was seen by Barrera-Pineda et al. (2002) from our data set. Instead, we attribute the strong emissivity variations to the Olbers structure and a neighbouring region.

5.2. Asteroid (9) Metis

As for (4) Vesta, the albedo uncertainty does not affect the flux prediction very much: the diameter is the dominant factor. The model input parameters and some results are given in Table 7. Based on these input parameters we obtained a 3180 μm flux density of 40 ± 4 mJy, depending on the above albedo/diameter combinations. Lowering the mm-emissivity to a value of 0.7 would give flux densities of 35 ± 3 mJy (averaged over one rotation period). An emissivity model as used for (4) Vesta produces rotational averaged fluxes of about 30 ± 3 mJy. The measured values favor therefore the solution with the lower emissivity, i.e., an emissivity of around 0.7 at mm-wavelengths. In Fig. 10 we show predictions for emissivities of 0.7 (solid line) and 0.6 (dashed line), which corresponds to (4) Vesta's emissivity model.

The predicted shape-introduced lightcurve variation under the given illumination and observing geometry is about ±2%. Figure 10 shows the predicted flux variation for the observed period in combination with the measurements from Table 4.

The measured lightcurve amplitude of about 24% peak-to-peak cannot be explained by the shape model. The thermal inertia has almost no effect on the lightcurve amplitude at these long wavelengths. Albedo spots can also be excluded as a cause for the large lightcurve amplitudes since the mm-emission is almost independent of albedo. The only possible reason seems to be that at certain rotational phases we see additional emission coming from subsurface layers, meaning that the regolith properties are inhomogeneous over the surface. Similar to the explanations for (4) Vesta, regions with young surface material with predominantly larger particle sizes could lower the emissivity

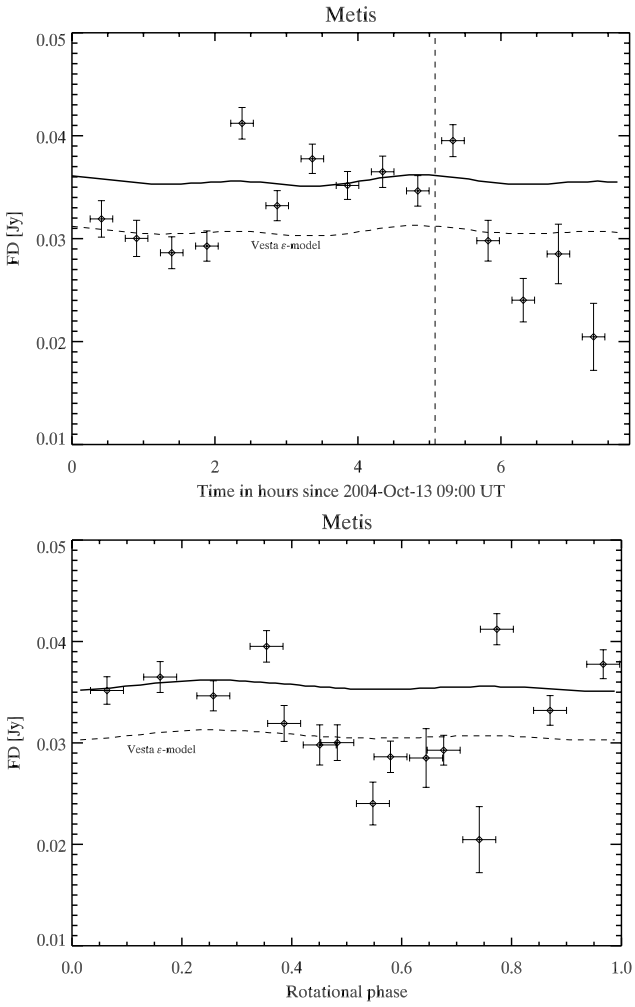

Fig. 10. *Top*: absolute flux prediction over time (solid line) together with the measurements (see Table 4). We used a wavelength-dependent emissivity model together with a size of 172 km and an albedo of 0.16. *Bottom*: the same as in the top, but now plotted against the rotational phase. The zero point in rotational phase is connected to the definition in Table 7. The dashed line indicates a model prediction with an emissivity of 0.6. This clearly shows the emissivity heterogeneity on the surface of (9) Metis. For the dashed lines we used the emissivity model for (4) Vesta.

significantly and produce very pronounced mm-lightcurve effects which would be seen at visual wavelengths. In fact, studies by Nakayama et al. (2000) and Storrs et al. (1999) indicated a heterogeneous surface for (9) Metis and the shape model (Torppa et al. 2003) has some sharp features, but the shape model fits nicely the available visual lightcurve without albedo variegations on the surface. Marchis et al. (2006) reported a bright structure in their Keck-AO images with a contrast of 20% in a Kp broadband filter (1.95–2.30 μm). This prominent surface marking was visible both images which were separated by about 2 h, taken at rotational phases of 0.42 and 0.81. These images were taken only a few days after our CA observations under a similar aspect angle. It might well be that this bright feature in reflectance has a significantly lower mm-emissivity than the rest of the surface and therefore this structure might cause the light-curve minimum in Fig. 10 (bottom) at rotational phases at around 0.55±0.15. The high contrast dark feature in the Keck image at rotational phase 0.81 might then be responsible for the abrupt flux change at the end of the lightcurve minimum in Fig. 10 (bottom).

6. Conclusion

The thermophysical model has been very successful in fitting the observed spectral energy distributions of main-belt asteroids across a wide range of wavelengths, from ~5 μm to ~1000 μm, namely across the brightest parts of their Planck functions (M&L 1998; 2002). At those wavelengths, the thermal behaviour is dominated by shape, albedo and thermal properties of the surface regolith. At millimetre-to-cm wavelengths albedo and thermal properties are less important and instead the emissivity of the surface material plays an important role. Especially the grain size distribution seems to lower the emissivity in the 90 GHz range and variations of the grain sizes apparently dominate the rotational flux changes. This has been the first serious test of the model at much longer wavelengths than those for which it was designed, and is therefore an opportunity not only to refine the model, but to learn more about the surface properties of these asteroids.

The emissivity of (4) Vesta and (9) Metis at the observed frequency range between 93 and 95.5 GHz is significantly lower than at wavelength ranges between the mid-IR and the submillimetre range. This can be explained by regolith properties which allow us to see colder layers below the surface. In other words, the grain sizes are comparable to the observing wavelength and internal reflection and scattering processes lower the emissivity in a wavelength-dependent fashion. Our measurements also show for the first time that surface heterogeneities affect the 3 mm-lightcurves dramatically. At shorter wavelengths below 1 mm, lightcurves are usually dominated by the object's shape. The simple existence of a surface regolith controls to a large extend the spectral energy distribution, but at 3 mm differences in regolith properties can be revealed and disentangled from the shape and albedo effects. Bright surface spots at visual or near-IR wavelengths seem to correspond to low emissivity parts in the 3 mm lightcurves. The very dark Olbers region on (4) Vesta might be the cause of an emissivity increase above the shape-introduced flux changes. Variations in emissivity at longer wavelengths – especially for (4) Vesta – need to be confirmed, in order to model regolith properties more rigorously. More observations of other targets, including also some lower albedo objects, are needed to establish possible relations between the albedo and the 3 millimetre emissivity. It would also be interesting to see if apparently homogeneous objects follow the predicted lightcurves or if they also show heterogeneities which are not present at visual and near-IR wavelengths. But such observations require stable conditions and careful calibration procedures during a significant part of the asteroid's rotation period. Along with other mm-interferometers, the ATCA has the potential to contribute significantly to these goals.

Acknowledgements. We would like to thank the ATNF TAC for the allocation of telescope time to an unusual project, and to the staff of the Compact Array for their usual outstanding help in meeting our goals. PJB gratefully acknowledges the Institute for Astronomy in the School of Physics at Sydney University for their support of the observations and analysis, and is also delighted to thank Yasuo Fukui and his NANTEN group at Nagoya University, for their hospitality during the conclusion of some of this work. We would also like to thank Mikko Kaasalainen for providing both shape models in an easily usable format and for support in the shape model implementation.

References

Barrera-Pineda, P. S., Lovell, A. J., Schloerb, F. P., & Carrasco, L. 2002, AAS, DPS#34, BAAS 34, 859
Binzel, R. P., Xu, S. 1993, Science, 260, 186
Binzel, R. P., Gaffey, M. J., Thomas, P. C. et al. 1997, Icarus, 128, 95
Drummond, J. D., Eckart, A., Hege E. K. 1988, Icarus, 73, 1
Griffin, M., & Orton, G. S. 1993, Icarus, 105, 537
Hansen, O. L. 1976, AJ 81, 74
Johnston, K. J., Lamphear, E. J., Webster, JR, W. J. et al. 1989, AJ, 98, 335
Kelley, M. S., & Gaffey, M. J. 2000, Icarus, 144, 27
Kutner, M. L., & Ulich, B. L. 1981, ApJ, 250, 341
Lagerkvist, C.-I., Piironen, J., & Erikson, A. 2001, Asteroid Photometric Catalogue, Fifth Update, Uppsala Astron. Obs.
Lagerros, J. S. V. 1996, A&A, 310, 1011
Lagerros, J. S. V. 1997, A&A, 325, 1226
Lagerros, J. S. V. 1998, A&A, 332, 1123
Lagerros, J. S. V., Müller, T. G., Klaas, U., & Erikson, A. 1999, Icarus, 142, 454
Lebofsky, L. A., Sykes, M. V., Tedesco, E. F., et al. 1986, Icarus, 68, 239
Marchis, F., Kaasalainen, M., Hom, E. F. Y., et al. 2006, Icarus, in press
Mitchell, D. L., Ostro, S. J., Rosema, K. D. et al. 1995, Icarus, 118, 105
Müller, T. G. 2002, M&PS 37, 1919
Müller, T. G., & Lagerros, J. S. V. 1998, A&A, 338, 340
Müller, T. G., & Lagerros, J. S. V. 2002, A&A, 381, 324
Müller, T. G., Lagerros, J. S. V., Burgdorf, M. et al. 1999, ESA SP-427, in The Universe as Seen by ISO, ed. P. Cox, & M. F. Kessler, 141
Nakayama, H., Fujii, Y., Ishiguro, M., et al. 2000, Icarus, 146, 220
Redman, R. O., Feldman, P. A., Matthews, H. E., Halliday, I., & Creutzberg, F. 1992, AJ, 104, 405
Redman, R. O., Feldman, P. A., & Matthews, H. E. 1998, AJ, 116, 1478
Sault, R. J., Teuben, P. J., & Wright, M. C. H. 1995, in Astronomical Data Analysis Software and Systems IV, ed. R. A. Shaw, H. E. Payne, & J. J. E. Hayes, ASP Conf. Ser. 77, 433
Shevchenko, V. G., & Tedesco, E. F. 2006, Icarus, 184, 211
Simpson, J. P., Cuzzi, J. N., Erickson, E. F., et al. 1981, Icarus, 48, 230
Storrs, A., Weiss, B., Zellner, B. et al. 1999, Icarus, 137, 260
Storrs, A. D., Dunne, C., Conan, J.-M., et al. 2005, Icarus, 173, 409
Tedesco, E. F. 1989, in Asteroids II, ed. G. Binzel, & M. Shapley (University of Arizona Press), 1090
Tedesco, E. F., Noah, P. V., Noah, M., & Price, S. D. 2002a, AJ, 123, 1056
Tedesco, E. F., Egan, M. P., & Price, S. D. 2002b, AJ, 124, 583
Thomas, P. C., Binzel, R. P., Gaffey, M. J. et al. 1997, Icarus, 128, 88
Torppa, J., Kaasalainen, M., Michalowski, T. et al. 2003, Icarus, 164, 346
Vernazza, P., Mothé-Diniz, T., Barucci, M. A. et al. 2005, A&A, 436, 1113
Webster, Jr., W. J., & Johnston, K. J. 1989, PASP, 101, 122
Zellner, B. H., Albrecht, R., Binzel, R. P. et al. 1997, Icarus, 128, 83